mater.scichina.com link.springer.com

Published online 22 November 2023 | https://doi.org/10.1007/s40843-023-2637-0
Sci China Mater 2023, 66(12): 4575–4586

Co_3O_4 nanosheets anchored on C/Cu porous microspheres as high-performance anode materials for lithium-ion battery

Xun Sun[1,2†], Jun Zhang[1†], Huaran Zhang[1], Yuliang Cao[1*] and Jinping Zhou[1*]

ABSTRACT **As electrode materials, transition metal oxides (TMOs) exhibit poor electrochemical performances owing to their inherent low electronic conductivity and considerable volume expansion and contraction during charge/discharge cycles. Designing TMOs with unique nanostructure and combining them with conductive carbon substrates are effective strategies to address the inherent issues. In this work, we designed C/Cu porous microspheres and grew Co_3O_4 nanosheets (NS) vertically on the carbon walls using an *in situ* synthesis route. As a conductive substrate, the C/Cu microspheres provide a hierarchical pore network and an electrode/electrolyte contact interface with large area, which can substantially enhance electron and ion diffusion kinetics. The *in situ* synthesized Co_3O_4 NSs are firmly anchored on the carbon walls, thereby increasing the structural durability of the composites in long-term cycling. Due to their unique structural characteristics, when using the C/Cu@Co_3O_4 composite microspheres as the anode materials for lithium-ion batteries, the batteries exhibit an enhanced rate performance (a high reversible specific capacity of 622 mA h g^{-1} at a current density of 5000 mA g^{-1}), high charge-specific capacity (907 mA h g^{-1} at 100 mA g^{-1} after 200 cycles, and a stable specific capacity of 944 mA h g^{-1} over 800 cycles, even at a high current density of 1000 mA g^{-1}), and excellent cycling stability.**

Keywords: C/Cu microspheres, multiscale pore structure, chitin-derived carbon, mesoporous Co_3O_4 nanosheets, anode materials

INTRODUCTION

With the growing interest in sustainable and renewable energy sources, the requirement for low-cost, efficient, and environment-friendly renewable energy conversion and storage technologies has become urgent [1,2]. Currently, lithium-ion batteries (LIBs) become the primary energy source for portable electronic devices. They are regarded as the most promising energy storage technology for grid applications and electric vehicles [3,4]. However, commonly used graphite anode materials cannot meet the rapidly growing demand for next-generation LIBs with high power and energy densities due to their low rate capability and low theoretical capacity. Therefore, extensive research is being conducted on alternative anode materials with high-rate performance and high capacity to develop a new generation of LIBs [5,6]. In this context, transition metal oxides (TMOs) are considered the most potential candidates for anode materials owing to their low cost, abundant natural resources, and theoretically high specific capacity [6–10]. Among various TMOs, Co_3O_4 is regarded as one of the most promising anode materials, which can provide a higher specific capacity (~890 mA h g^{-1}) owing to its eight-electron transfer reaction compared with the conventional graphite anode [11,12]. However, Co_3O_4 has two major drawbacks. One is that during the charge/discharge cycling process, severe volume changes in the active material result in electrode shattering and poor long-cycling stability. The other is that the inherent low electronic conductivity of Co_3O_4 leads to poor rate performance. These issues seriously impede its practical applications in LIBs [13,14].

Two effective strategies have been extensively investigated to address the aforementioned obstacles and enhance the lithium storage capacity of Co_3O_4-based electrodes. One approach is to design unique Co_3O_4 nanostructures, such as nanoparticles [15,16], nanotubes [17,18], nanorods [19], hollow nanospheres [20,21], nanoflowers [22,23], and nanosheets (NS) [24,25]. These nanostructures render the active material a larger specific surface area, enlarge the electrolyte/electrode contact interface, shorten the transport distance of Li^+, and consequently enhance the diffusion kinetics. Furthermore, nanostructures, particularly porous or hollow structures, can reduce the volume expansion/contraction during Li^+ insertion/extraction to a certain extent [26,27]. However, during the charging and discharging processes, the nanostructured Co_3O_4 often suffers from severe particle aggregation, large volume changes, and low conductivity, which leads to electrode crushing and rapid capacity decay, thereby presenting poor long-term cycling stability and rate performance [28,29]. The other efficient strategy is to introduce a specific conductive buffer matrix, such as graphene [30,31], carbon nanotubes [32], carbon nanofibers [33], and porous carbon [34,35], to form corresponding Co_3O_4 composites. Carbon materials can provide a fast electron conduction channel, which improves the conductivity of the active material. Moreover, the carbon material can buffer the volume change during the charge/discharge cycles, and effectively prevent the aggregation of nanoparticals [36]. Thus, stable specific reversible capacity and good rate capability could be achieved. In this

[1] Hubei Engineering Center of Natural Polymer-based Medical Materials, Engineering Research Center of Organosilicon Compounds & Materials of Ministry of Education, Department of Chemistry, Wuhan University, Wuhan 430072, China
[2] College of Material Engineering, Xuzhou Vocational College of Industrial Technology, Xuzhou 221000, China
† These authors contributed equally to this work.
* Corresponding authors (emails: zhoujp325@whu.edu.cn (Zhou J); ylcao@whu.edu.cn (Cao Y))

context, Zhang *et al.* [37] prepared a high-density corn-like Co_3O_4/graphene hybrid material by direct pyrolysis of $Co(NO_3)_2{\cdot}6H_2O$ on graphene NS through self-assembly induced by graphene wrinkles. This composite preserved a high reversible capacity of 1060 mA h g^{-1} after 50 cycles at a current density of 50 mA g^{-1}. Chen *et al.* [38] reported a nanocomposite material of Co_3O_4 nanoparticles grafted onto a three-dimensional (3D) nanotube sponge. The material exhibited an excellent rate capability and a high specific capacity. However, achieving a strong interaction between Co_3O_4 and carbon substrates and thus avoiding the shedding and aggregation of nanomaterials during repeated lithiation/delithiation processes remain challenging.

Chitin is the second largest amount of biomass on Earth. Direct pyrolysis is used to uniformly incorporate heteroatoms into the carbon structure of chitin, resulting in N/O self-doping. This material has been reported as an anode material for high-performance electrode materials [33,39,40]. Recently, we developed a dissolution system for chitin based on alkali/urea aqueous solutions and constructed heteroatom-self-doped C/Cu composite porous microspheres using an emulsion method and high-temperature carbonization [41]. The composite microspheres are robust with abundant anchoring sites. Herein, we innovatively constructed C/Cu composite microspheres, which are uniformly covered with Co_3O_4 NS on the carbon wall (C/Cu@Co_3O_4), as a high-performance anode material for LIBs. Combining the advantages of vertically aligned mesoporous Co_3O_4 NS and heteroatom-self-doped C/Cu porous microspheres as conductive substrates, the prepared C/Cu@Co_3O_4 hybrids demonstrate excellent lithium storage performance when used as the anode materials for LIBs, with high reversible capacity, excellent rate performance, and long-cycle life. Therefore, this work provides a new strategy for developing high-performance anode materials for LIBs based on carbon/TMO composites.

EXPERIMENTAL SECTION

Raw materials

Chitin was procured from Golden Shell Biochemical Co., Ltd. (Zhejiang, China) and processed following the previous work [42]. Cobalt acetate tetrahydrate, polyvinylpyrrolidone (PVP), and $Cu(OH)_2$ were obtained from Aladdin (Shanghai, China). All other chemical reagents used in the experiments were procured from Sinopharm (Shanghai, China) and used without further purification.

Preparation of C/Cu porous microspheres

As reported in our previous work [41], we developed a stable $Na_2[Cu(OH)_4]$/NaOH/urea system to dissolve chitin based on the alkali/urea solvent system. In this system, chitin was dissolved using the freeze-thaw method to accomplish uniform blending of $Na_2[Cu(OH)_4]$ and polymeric chains to obtain a chitin solution. Then, chitin@$Cu(OH)_2$ microspheres were prepared using the emulsion method, and finally, the freeze-dried chitin@$Cu(OH)_2$ microspheres were carbonized at high temperature to obtain C/Cu composite porous microspheres.

Preparation of C/Cu@Co_3O_4 microspheres

Cobalt acetate tetrahydrate (2.0 g) and PVP (0.8 g) were added into 60 mL of a mixture of ethylene glycol (EG) and deionized water (volume ratio = 59:1) and stirred for 30 min to obtain a burgundy solution. After adding 1.0 g of C/Cu porous microspheres into the burgundy solution, it was stirred for 8 h. Then, the mixture was transferred into a 100-mL autoclave and placed in a muffle furnace at 180°C for 12 h. The precipitates were collected after cooling to room temperature, washed several times with deionized water and anhydrous ethanol, and dried under vacuum at 60°C for 12 h. Finally, the resulting precursor was heated at 400°C under argon for 2 h, and C/Cu microspheres loaded with Co_3O_4 NS (C/Cu@Co_3O_4) were obtained. Conversely, pure Co_3O_4 NSs were prepared without adding C/Cu microspheres, while other parameters remained constant.

For comparison, C/Cu microspheres were oxidized in air at 300°C with a heating rate of 2°C min^{-1} for 3 h to produce C/CuO microspheres. The C/CuO microspheres were added to a dilute HCl solution with stirring for enough time to remove the CuO, obtaining bare carbon microspheres (CMs). Then, we replaced C/Cu with CMs and synthesized CMs@Co_3O_4 using the same solvothermal reaction under the same conditions.

Characterizations

The morphology and structure of the samples were analyzed using scanning electron microscopy (SEM, FEI SIRION-200) and transmission electron microscopy (TEM, JEOLJEM-2010 (HT)) coupled with an energy dispersive X-ray spectrometer (EDS, Super-X). Powder X-ray diffraction (XRD) was performed using a Rigaku Miniflex600 X-ray powder diffractometer with Cu Kα radiation. X-ray photoelectron spectrometry (XPS) was conducted using an ESCALAB 250Xi spectrometer. Thermogravimetric (TG) analyses were conducted on a TA Q500 instrument in an air atmosphere with a ramp rate of 10°C min^{-1}. A Micromeritics ASPA 2020 analyzer was used to measure the N_2 adsorption/desorption isotherms and pore size distribution of the samples. The Raman spectra were acquired with a Renishaw RM1000 spectrometer.

Electrochemical characterization

The active materials (C/Cu@Co_3O_4 microspheres and the pure Co_3O_4 NS), carboxymethyl cellulose, and Super P were mixed in deionized water with a mass ratio of 70:20:10 to prepare a slurry. The slurry was then uniformly applied on the copper foil using a sample maker and vacuum dried at 60°C for 12 h to fabricate electrode sheets. The average mass loading of the electrodes was 1.5 mg cm^{-2}. For constructing the 2032-coin cell, the obtained electrode sheet served as the working electrode, the metal Li sheet as the reference electrode, and the glass fiber membrane as the diaphragm. The electrolyte was a mixture of ethyl methyl carbonate, dimethyl carbonate, and ethylene carbonate (volume ratio of 1:1:1) in 1 mol L^{-1} $LiPF_6$. The button cells were assembled in an argon-filled glove box where the concentrations of O_2 and H_2O were less than 0.01 ppm, respectively. The assembled cells standed for at least 12 h before testing to allow sufficient electrolyte penetration into the electrodes.

The LAND-CT2011A battery measurement system measured the galvanostatic charge/discharge (GCD) curves from 0.01–3 V. The CHI660E electrochemistry workstation (Shanghai Chenhua) was used to conduct cyclic voltammogram (CV) and electrochemical impedance spectroscopy (EIS) measurements. CV measurements were done from 0.01–3 V at a scan rate of 0.2–5 mV s^{-1} and EIS measurements were assessed at a frequency range from 0.01–100 kHz. All the electrochemical measure-

ments were performed at 25°C.

RESULTS AND DISCUSSION

Preparation and structural analysis

Fig. 1 presents a schematic diagram of the preparation of C/Cu@Co_3O_4 composite microspheres. We first prepared the chitin-$Na_2[Cu(OH)_4]$ solution using multiple freeze-thawing processes and then added it dropwise into the oil phase comprising isooctane and Span 85 as the aqueous phase. Chitin@$Cu(OH)_2$ microspheres were prepared using emulsification and high-temperature regeneration, and then, C/Cu porous microspheres were obtained by high-temperature carbonization. Subsequently, we synthesized cobalt glycolate precursors using an EG-mediated solvothermal method, where PVP and water were used to control the morphology of cobalt glycolate NSs. Finally, C/Cu@Co_3O_4 composite microspheres were obtained by calcination in an argon atmosphere.

The surface of the prepared chitin@$Cu(OH)_2$ microspheres shows a distinct porous structure (Fig. 2a), and the average diameter is 70 ± 4 μm. Furthermore, the resulting C/Cu microspheres still maintain a good spherical morphology even after carbonization in argon at 800°C; however, the average diameter decreases to 25 ± 7 μm, and their porous structure increases (Fig. 2b). The XRD pattern of C/Cu (Fig. S1) depicts that there are distinct diffraction peaks at 2θ = 43.4°, 50.4°, and 74.1°, which correspond to the (111), (200), and (220) crystal planes of Cu (PDF#70-3039), respectively. A very weak (002) diffraction peak appears at 2θ = 24.3°, demonstrating the amorphous nature of the carbon matrix. Under high temperature, $Cu(OH)_2$ in chitin@$Cu(OH)_2$ microspheres is first thermally decomposed to CuO, while chitin-derived carbon acts as a reducing agent to reduce CuO to Cu. During this period, chitin and its derived carbon skeleton also serve as substrates to prevent the aggregation of Cu nanoparticles [43].

The final hydrothermal reaction and calcination treatment did not considerably affect the size and morphology of the microspheres. The obtained C/Cu@Co_3O_4 composite microspheres still exhibit a good spherical shape with an average diameter of 28 ± 5 μm (Fig. 2c). According to the SEM images (Fig. S2a, b), the surface of the C/Cu@Co_3O_4 microsphere is covered by interlaced Co_3O_4 NS. Moreover, the SEM cross-sectional images show the broken microsphere (Fig. S2c, d), which indicates that the carbon walls of the internal channels of the microspheres are covered with Co_3O_4 NS. Thus, we found that Co_3O_4 NS are evenly distributed on the surface of the microspheres and grow on the carbon walls of the microsphere internal channels. Notably, the *in situ* synthesized Co_3O_4 NS do not substantially affect the structure of C/Cu. The TEM image (Fig. 2d) depicts that the inside of the C/Cu@Co_3O_4 microspheres still has a rich porous structure. Furthermore, thin flake-like materials appear at the edges of the microspheres, which are Co_3O_4 NS wrapping around the surface of the C/Cu@Co_3O_4 microspheres. Fig. 2e depicts the high-resolution TEM (HRTEM) image of the Co_3O_4 NS. A lattice spacing of 0.23 nm was calculated between two neighboring planes, which is attributed to the (222) lattice plane of Co_3O_4. The elemental mapping images of C/Cu@Co_3O_4 were examined using high-angle annular dark field scanning TEM-EDS (HAADF-STEM-EDS) (Fig. 2f–k), showing uniform distributions of C, O, N, Cu, and Co in the selected region.

Fig. S3 shows the SEM image of the pure Co_3O_4 precursor as a stack of NS with a smooth surface. After calcination in argon, Co_3O_4 NS with mesopores were obtained (Fig. S4a, b), while the residual carbon content of the Co_3O_4 NS was minimal after subsequent washing. This was confirmed by the XRD pattern of Co_3O_4 NS (Fig. S5), as no significant carbon (002) diffraction peaks were observed at around 24°. The distinct diffraction peaks identified at 2θ = 19.1°, 31.3°, 36.9°, 38.6°, 44.9°, 55.8°, 59.5°, 65.3°, and 77.6° correspond well with the (111), (220), (311), (222), (400), (422), (511), (440), and (533) Co_3O_4 planes,

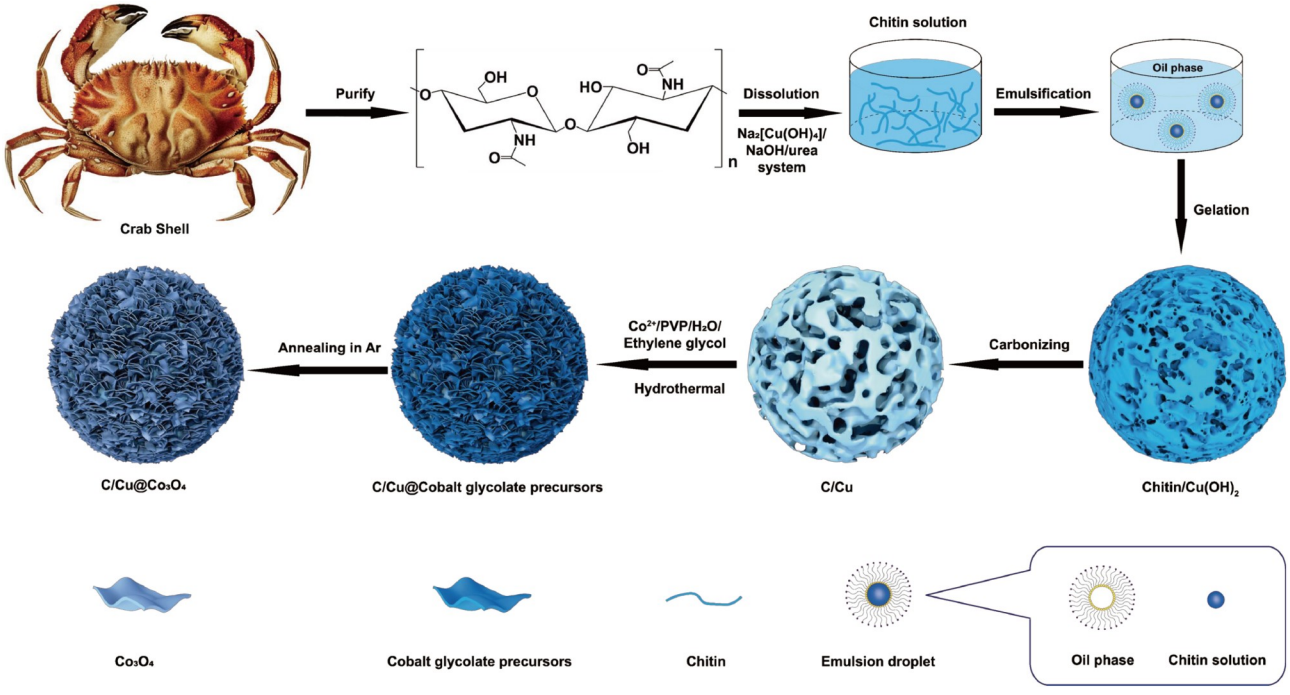

Figure 1 Schematic diagram for the fabrication of C/Cu@Co_3O_4 composite microspheres.

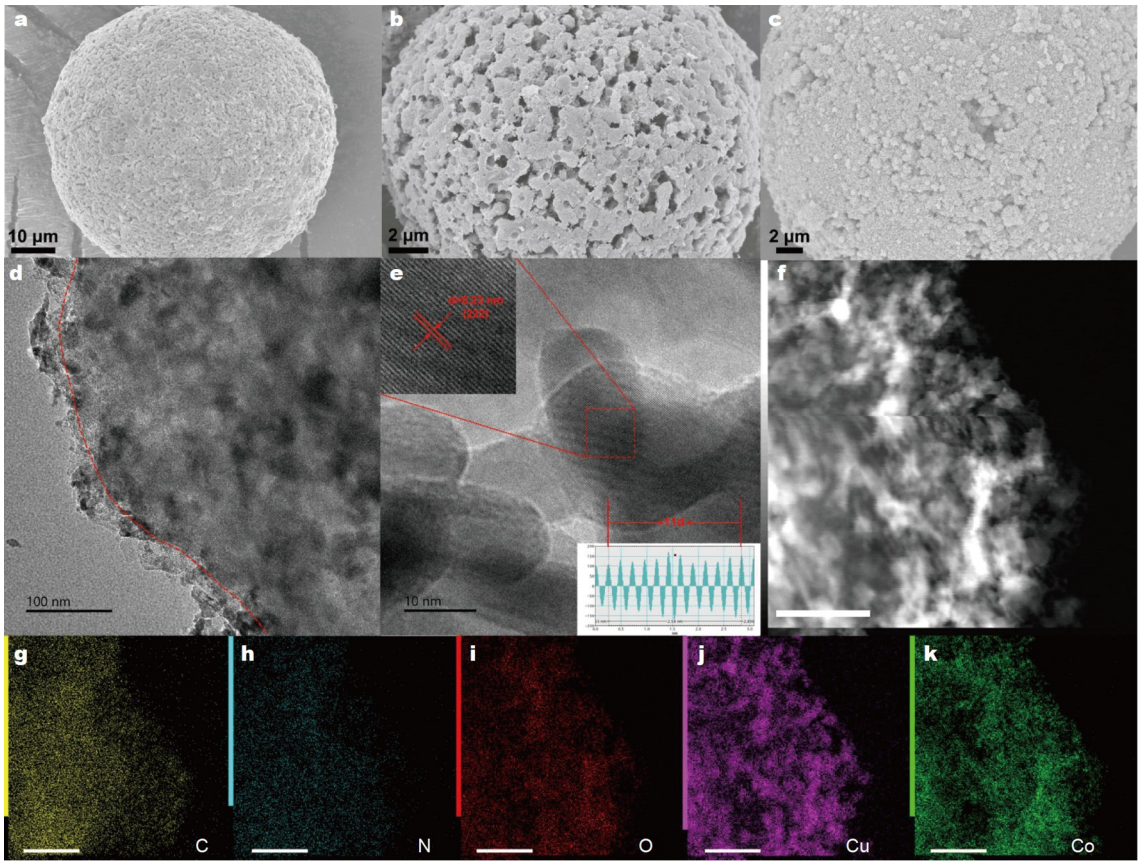

Figure 2 SEM images of (a) chitin@Cu(OH)$_2$, (b) C/Cu, and (c) C/Cu@Co_3O_4. (d) TEM and (e) HRTEM images of C/Cu@Co_3O_4 (insets: the crystalline lattice pattern and the corresponding intensity profile of a line scan across the lattice fringes). (f) HAADF-STEM image and (g–k) the corresponding element mappings of C/Cu@Co_3O_4. The scale bars are 200 nm.

respectively (PDF#42-1467). Raman spectrum of Co_3O_4 NS further reveals the characteristic peaks of Co_3O_4 (Fig. S6). Five diffraction peaks at 196, 480, 518, 617, and 682 cm^{-1} can be indexed to F_{2g}, E_g, F_{2g}^1, F_{2g}^2, and A_{2g}^1 vibration models of Co_3O_4 [35], respectively. The absence of distinct D and G bands in the Raman spectrum of Co_3O_4 NS further confirms the very low carbon content that could not be detected. Considering the morphology reported in the literature [44,45], we deduced the growth mechanism of Co_3O_4 NS on C/Cu porous microspheres. First, Co^{2+} are coordinated with EG under constant magnetic stirring to create cobalt glycolate. Then, as the temperature rises, PVP and cobalt glycolate in the solution start to react and nucleate uniformly on the carbon walls of the C/Cu microspheres. The presence of water may reduce the coverage of PVP on the surface of NS, resulting in preferential absorption of PVP on the top surfaces of NS. As the reaction progresses, nuclei form preferentially in a particular direction to form NS. Finally, the obtained precursors are calcined in argon, and Co_3O_4 NS arrays are prepared with the pores grown vertically on the carbon walls of C/Cu microspheres.

Fig. S7 displays the curves obtained from specific surface tests on Co_3O_4 NS to characterize their pore structure. The N_2 adsorption/desorption curves of Co_3O_4 NS exhibit a clear hysteresis loop between P/P_0 values of 0.4–1.0, which indicates a distinct type IV isotherm. Moreover, this hysteresis loop is evidence for the presence of mesopores. The uptake of N_2 by Co_3O_4 NS increases substantially at the relative pressure of $P/P_0 > 0.9$, indicating the existence of macropores. However, at the relative pressure of $P/P_0 < 0.1$, the adsorption of N_2 by Co_3O_4 NS is almost unchanged, indicating the absence of micropores [46]. The specific surface area of Co_3O_4 NS is 8.5 $m^2\ g^{-1}$, and the corresponding pore volume is 0.045 $cm^3\ g^{-1}$. The pore size distribution shows that the mesoporous structure of Co_3O_4 NS is predominant, and the related results are given in Table S1. The mesoporous structure of Co_3O_4 NS facilitates electrolyte penetration and relieves volume expansion/contraction during the charging/discharging cycles, thereby guaranteeing its structural integrity.

Fig. 3a shows the XRD pattern of C/Cu@Co_3O_4. The distinct diffraction peaks at 2θ = 18.8°, 31.1°, 36.7°, 38.2°, 44.8°, 55.8°, 59.2°, 65.2°, and 77.5° are attributed to (111), (220), (311), (222), (400), (422), (511), (440), and (533) Co_3O_4 planes, respectively (PDF#42-1467). The characteristic diffraction peaks of Cu were also observed. Furthermore, the amount of Co_3O_4 in C/Cu@Co_3O_4 microspheres can be calculated from the TG curves of C/Cu and C/Cu@Co_3O_4 microspheres in the air (Fig. 3b). During the gradual heating to 800°C in an air atmosphere, Cu is oxidized to CuO in the presence of air and later reduced to Cu by C for C/Cu microspheres. Until the C is completely burned out, Cu will finally exist as CuO. Similarly, for C/Cu@Co_3O_4, after heating to 800°C in an air atmosphere, the final residues become CuO and Co_3O_4. The specific reaction can be briefly

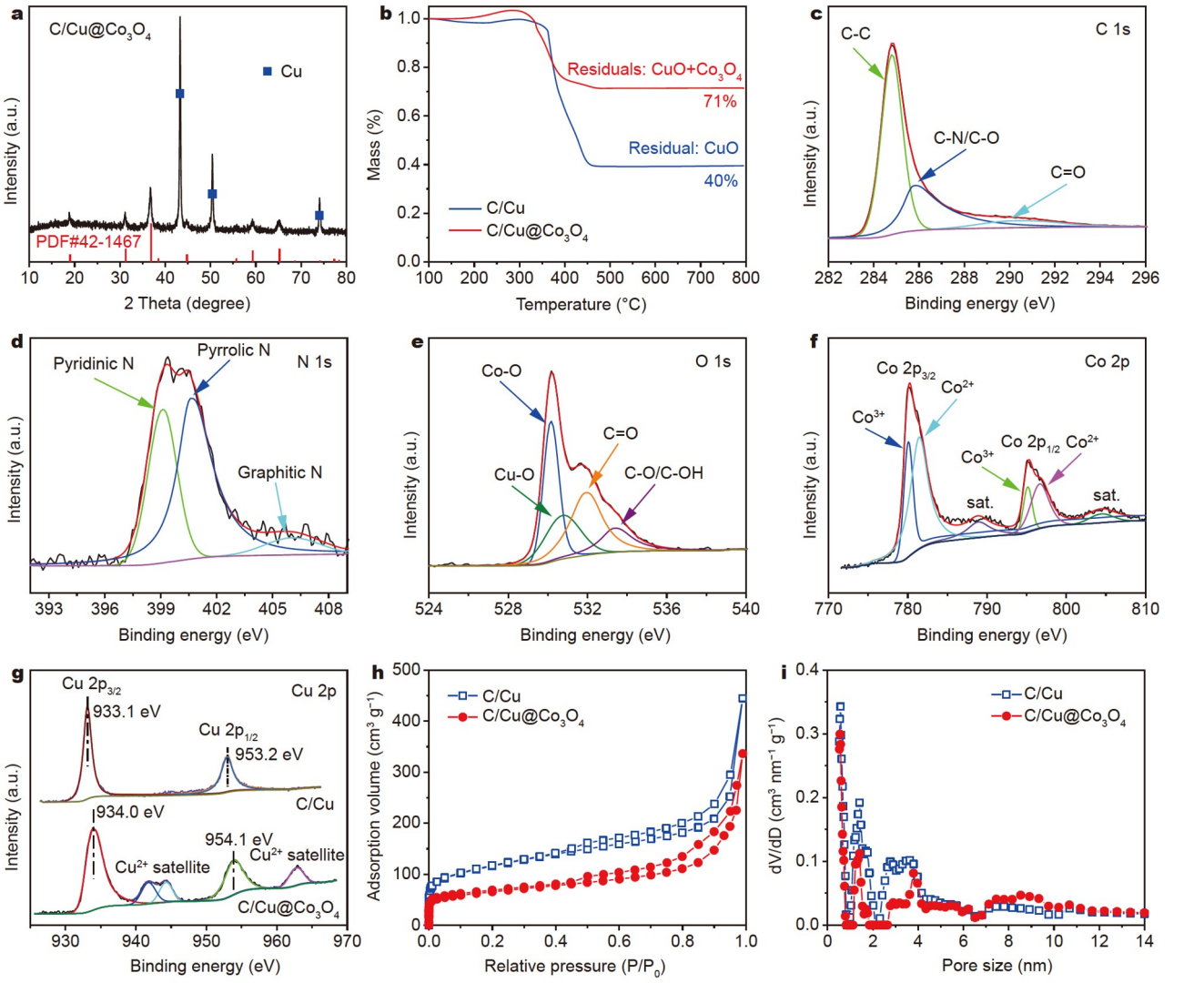

Figure 3 (a) XRD pattern of C/Cu@Co_3O_4, and (b) TG curves of C/Cu and C/Cu@Co_3O_4 in air. XPS spectra of C/Cu@Co_3O_4: (c) C 1s, (d) N 1s, (e) O 1s, and (f) Co 2p. (g) Cu 2p XPS spectra of C/Cu and C/Cu@Co_3O_4. (h) N_2 adsorption/desorption isotherms of C/Cu and C/Cu@Co_3O_4, and (i) the corresponding DFT pore size distributions.

summarized as follows:

$$2C/Cu + 3O_2 \rightarrow 2CuO + 2CO_2, \quad (1)$$

$$2C/Cu@Co_3O_4 + 3O_2 \rightarrow 2CuO + 2Co_3O_4 + 2CO_2. \quad (2)$$

The TG curve of C/Cu indicates that the mass of the remaining CuO is about 40%. According to the TG curve of C/Cu@Co_3O_4, the mass fraction of the remaining residues (CuO and Co_3O_4) is 71%. Therefore, the Co_3O_4 content was calculated to be 52% in C/Cu@Co_3O_4, and the composite microspheres prepared in this work achieved a high loading of TMOs.

Fig. S8 displays the XPS spectrum of C/Cu@Co_3O_4 microspheres, from which distinctive characteristic peaks of C 1s, N 1s, O 1s, Co 2p, and Cu 2p are observed, showing their coexistence. Fig. 3c presents the high-resolution XPS spectrum of C 1s fitted to C–C (284.8 eV), C–N/C–O (285.8 eV), and C=O (290.1 eV) [47]. The high-resolution XPS spectrum of N 1s (Fig. 3d) shows three fitted peaks at 399.1, 400.1, and 406.1 eV, which correspond to pyridinic N, pyrrolic N, and graphitic N [48], respectively. In the high-resolution XPS spectrum of O 1s (Fig. 3e), peaks with binding energies of 530.2, 530.9, 532.0, and 533.5 eV are attributed to Co–O, Cu–O, C=O, and C–O/C–OH [49], respectively. The two prominent peaks at 780.3 and 795.3 eV in the high-resolution Co 2p XPS spectrum of C/Cu@Co_3O_4 (Fig. 3f) correspond to the spin-orbit peaks of Co $2p_{3/2}$ and Co $2p_{1/2}$, respectively, and are accompanied by two low-intensity swinging satellite peaks next to each other. The Co 2p peaks are characteristics of the Co_3O_4 phase [50]. The fitted peaks at 780.1 and 795.2 eV correspond to Co^{3+} $2p_{3/2}$ and Co^{3+} $2p_{1/2}$, respectively. The other two fitted peaks at 781.5 and 796.7 eV are assigned to Co^{2+} $2p_{3/2}$ and Co^{2+} $2p_{1/2}$ [51], respectively. Fig. 3g demonstrates the high-resolution Cu 2p XPS spectra of C/Cu and C/Cu@Co_3O_4. For C/Cu, the peaks at 933.1 and 953.2 eV are attributed to Cu $2p_{3/2}$ and Cu $2p_{1/2}$ of the Cu [52], respectively. Simultaneously, the Cu 2p spectrum of C/Cu does not have the satellite, which indicates the absence of Cu^{2+}. Conversely, two spin-orbiting doublets and two shaking satellites can be detected in the spectrum of C/Cu@Co_3O_4. Although the peaks at 934.0 and 954.1 eV are 0.9 eV higher than the binding energies of the corresponding peaks in C/Cu, they are also attributed to Cu $2p_{3/2}$ and Cu $2p_{1/2}$ of Cu. The increase in Cu

2p binding energy in C/Cu@Co_3O_4 reflects the reduction in charge density at the Cu site. However, the positive shift in binding energy may be attributed to the formation of Cu–O–Co bonds between the Co_3O_4 NS and Cu in the carbon matrix [53]. Moreover, the presence of Cu^{2+} satellite peaks (941.8, 944.3, and 963.0 eV) in the XPS spectrum of Cu 2p confirms the presence of covalent interactions between Cu and Co_3O_4 NS in the C/Cu@Co_3O_4 microspheres [54].

The porous structures of C/Cu and C/Cu@Co_3O_4 microspheres were analyzed using the Brunauer–Emmet–Teller theory, and the results are presented in Fig. 3h, i and Table S1. All the N_2 adsorption/desorption isotherms exhibit a distinct hysteresis loop between P/P_0 values of 0.4–1.0, suggesting a distinct type IV isotherm. Also, the existence of the mesopore is demonstrated by the hysteresis loop. The uptake of N_2 by C/Cu or C/Cu@Co_3O_4 increases substantially at the relative pressures of $P/P_0 < 0.1$ and $P/P_0 > 0.9$, indicating the existence of micropores and macropores, respectively [46]. The specific surface areas of C/Cu and C/Cu@Co_3O_4 are 420.5 and 278.6 $m^2\ g^{-1}$, whereas the corresponding total pore volumes are 0.70 and 0.52 $cm^3\ g^{-1}$, respectively. The pore size distribution calculated using the density functional theory (DFT) method indicates the dominance of micro- and mesoporous structures in C/Cu and C/Cu@Co_3O_4, with average pore sizes of 7.2 and 4.4 nm, respectively. The hierarchical structure of the composite microsphere provides a large specific surface area and interconnected pores network, which contributes to adapting to huge volume changes during charging/discharging processes, improves electron conductivity, and promotes ion transport and fast reactions.

To demonstrate that the presence of Cu in C/Cu microspheres provides nucleation sites for the growth of Co_3O_4 NS, the pure porous CMs were prepared. The SEM image in Fig. S9 shows the surface morphology of CMs similar to that of C/Cu. Based on the previous analysis of the specific surface area and pore size distribution of C/Cu microspheres, the N_2 adsorption/desorption curve (Fig. 4a) indicates that CMs have a hierarchical pore structure with the coexistence of micro-/meso-/macropores, as confirmed by their pore size distribution curve (Fig. 4b). The XPS spectrum and XRD pattern (Fig. 4c, d) prove that Cu is completely removed from CMs. Under the same conditions, the CMs@Co_3O_4 microspheres were prepared by solvothermal reaction using CMs as the substrate. The SEM image in Fig. S10 shows the absence of Co_3O_4 NS on the surface of CMs microspheres, indicating the presence of Cu in C/Cu microspheres is a critical factor for the nucleation and growth of Co_3O_4 NS.

Electrochemical properties

The electrochemical performances of C/Cu@Co_3O_4 as an anode material for LIBs were assessed. The lithium storage performance of Co_3O_4 NS was likewise evaluated to demonstrate its structural superiority. Fig. 5a depicts the CV curves of the C/Cu@Co_3O_4 electrode for the first four cycles at a scan rate of 0.2 mV s^{-1} within a voltage window of 0.01–3.00 V. During the first cathode scan, three reduction peaks were found at 1.54, 0.73, and 0.52 V, corresponding to the reduction of Co_3O_4 to CoO, the reduction of CoO to Co, and the formation of the solid

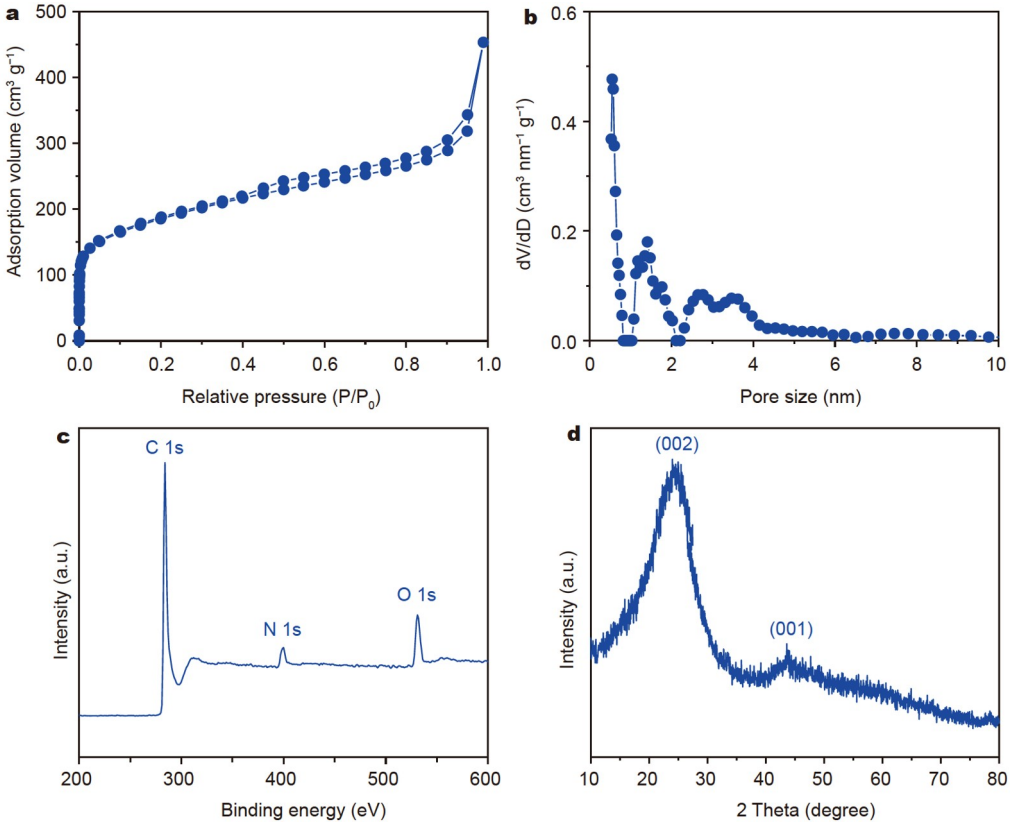

Figure 4 (a) N_2 adsorption/desorption isotherm and (b) the corresponding DFT pore size distribution. (c) Full survey XPS spectrum and (d) XRD pattern of CMs.

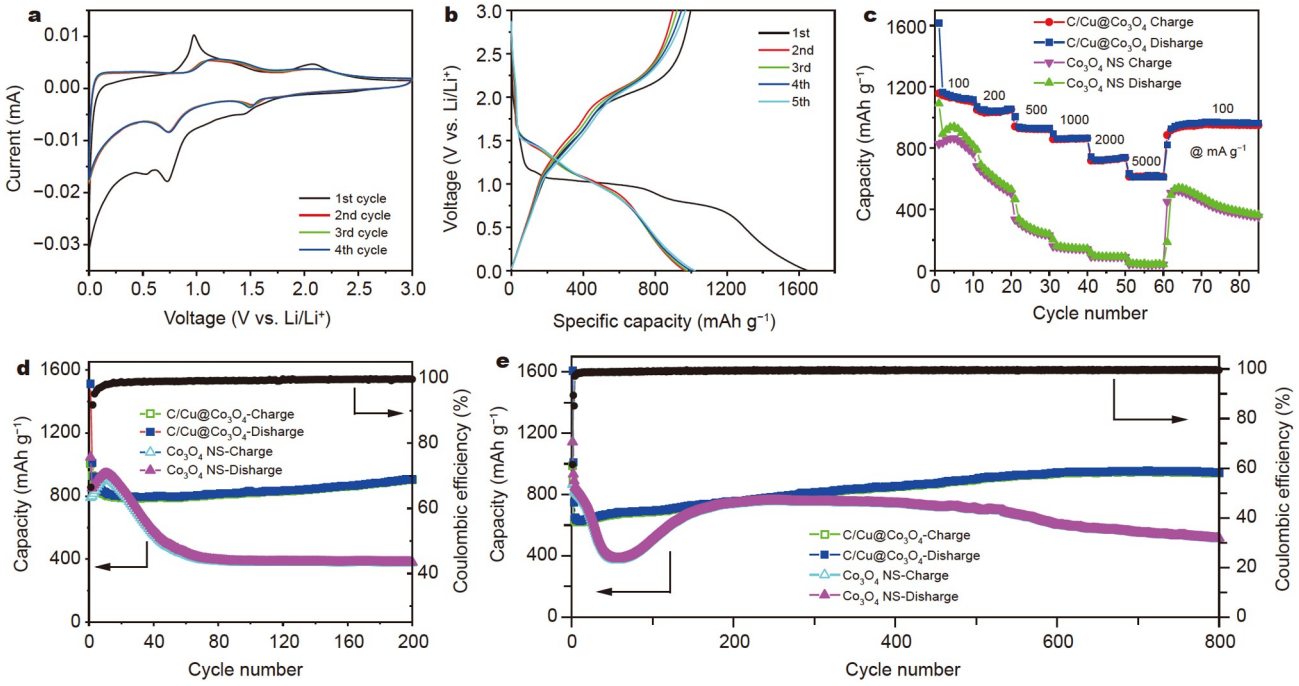

Figure 5 (a) The first four CV curves of the C/Cu@Co_3O_4 electrode over a potential range of 0.01–3.0 V at a scan rate of 0.2 mV s^{-1}. (b) GCD curves of the first five cycles of the C/Cu@Co_3O_4 electrode at a current density of 100 mA g^{-1}. (c) Rate performances of the C/Cu@Co_3O_4 and Co_3O_4 NS electrodes at various current densities. Cycling performances and the corresponding Coulombic efficiency of the C/Cu@Co_3O_4 and Co_3O_4 NS electrodes at (d) 100 and (e) 1000 mA g^{-1}.

electrolyte interface (SEI) [35], respectively. The electrochemical reaction mechanism of Co_3O_4 includes the formation and decomposition of Li_2O, the reduction of Co^{3+} to Co^{2+} and Co^{2+} to Co, and the oxidation of Co to Co^{2+} and Co^{2+} to Co^{3+}, with CoO as an intermediate product. The specific reaction can be expressed as follows [55]:

$$Co_3O_4 + 2Li^+ + 2e^- \rightarrow Li_2O + 3CoO, \quad (3)$$

$$3CoO + 6Li^+ + 6e^- \rightarrow 3Li_2O + 3Co. \quad (4)$$

During the first anodic cycle, distinct oxidation peaks were found at 0.98 and 2.08 V, corresponding to the oxidation of Co and the decomposition of Li_2O [33], respectively. In the second scan, the positions of both the reduction and oxidation peaks are shifted. This is a typical phenomenon of structural changes in metal oxides during charge/discharge cycles. The decrease in the integrated area and intensity of individual peaks signifies the loss of capacity and the formation of SEI films in the first cycle [56]. Following that, the positions of the reduction and oxidation peaks in the subsequent three cycles almost overlap. Except for the first cycle, the almost overlapping CV curves demonstrate the high reversibility of the redox reaction on the C/Cu@Co_3O_4 electrode and the exceptional cyclic stability of the cell owing to its unique structure.

Fig. 5b depicts the GCD curves recorded between 0.01 and 3.00 V at a current density of 100 mA g^{-1}. During the first discharge cycle, three voltage platforms appear between 1.5 and 0.5 V, attributing to the reaction of Li^+ insertion into Co_3O_4 and the creation of irreversible SEI layers. The initial discharge and charge-specific capacities are 1653 and 998.5 mA h g^{-1}, respectively, with an initial Coulomb efficiency of about 60%, and the inevitable capacity loss can be ascribed to the creation of SEI layers and incomplete insertion of Li in the electrodes [57]. In the next discharge curve, only two discharge voltage platforms are observed at around 1.5 and 0.75 V, corresponding to the reaction of Li^+ insertion into Co_3O_4. During the charging processes, two distinct voltage platforms can be observed at about 1.1 and 2.1 V, which are attributed to the recombination of Co and Li_2O into Co_3O_4 and Li^+ [58], respectively. The discharge- and charge-specific capacities of the second cycle are 967.6 and 902.3 mA h g^{-1}, respectively, with a corresponding Coulomb efficiency of 93%. Moreover, the reversible specific capacity of C/Cu@Co_3O_4 gradually increases from the second cycle onward. The increase in reversible capacity during the discharge/charge cycles is a characteristic feature of the metal oxide anode materials. This can be explained by the gradual activation processes and the reversible reaction of the polymer gel-like film between the metal particles and the electrolyte [58,59].

The C/Cu@Co_3O_4 electrode exhibits an excellent rate performance at various discharge/charge current densities. As illustrated in Fig. 5c, the C/Cu@Co_3O_4 electrode exhibits high average charging capacities of 1140, 1050, 938, 867, 730, and 616 mA h g^{-1} at the current densities of 100, 200, 500, 1000, 2000, and 5000 mA g^{-1}, respectively. Even after discharge/charge processes at different current densities, the C/Cu@Co_3O_4 electrode could maintain a stable and high charge-specific capacity of ~970 mA h g^{-1} when the current density was dropped to 100 mA g^{-1} again, suggesting the superior cyclic stability and reversibility of the electrode. However, in contrast, the pure Co_3O_4 NS electrode exhibits low reversible specific capacity, poor rate performance, and cycling stability. Furthermore, the discharge/charge curves of the C/Cu@Co_3O_4 electrode show a significant sloping plateau at different current densities (Fig. S11), attributing to the combined diffusion-controlled and capacitive-controlled lithium storage mechanisms (Fig. S12).

The cycle performance of the C/Cu@Co_3O_4 electrode was examined at current densities of 100 and 1000 mA g^{-1}. The results of the Co_3O_4 NS electrode were compared under identical conditions as a control. Fig. 5d illustrates the cycling process of the electrode at 100 mA g^{-1} with an initial discharge and charge capacity of 1511.2 and 1004.5 mA h g^{-1} for the C/Cu@Co_3O_4 electrode, respectively, with an initial Coulomb efficiency of 66.5%. During the next cycles, the Coulomb efficiency gradually increases, reaches more than 98% after several cycles, and remains stable, indicating a high cycle reversibility during the charging/discharging processes. Throughout the cycles, we observed that the specific capacity of the C/Cu@Co_3O_4 electrode decreased slightly during the first 20 cycles and then gradually increased to a relatively stable value. The decay of capacity in the early stage is attributed to the volume expansion/contraction caused by the Li^+ insertion/extraction processes, leading to the continuous formation of SEI films on the new surface. As charging and discharging cycles progress, the SEI films of Co_3O_4 NS tend to stabilize quickly. The presence of an adequate gap between Co_3O_4 NSs that are immobilized on the C/Cu substrate can effectively prevent the hierarchical structure from collapsing and splitting [12]. The latter phenomenon of capacity increase is common during the charge/discharge cycles of metal oxide anode materials. This can be explained by the gradual activation processes of the metal oxide and the reversible reaction of the polymer gel-like film between the metal particles and the electrolyte [58,59]. The discharge/charge cycling curve of the Co_3O_4 NS electrode exhibits an increasing trend followed by a subsequent decline. Finally, only 381 mA h g^{-1} of the charge-specific capacity is retained after 200 cycles at a current density of 100 mA g^{-1}. The increase in capacity during the first 10 cycles of the Co_3O_4 NS electrode can be explained by its gradual activation. The rapid decay of capacity in the later cycles may be due to the aggregation and crushing of Co_3O_4 NS during the cycling process [60]. The vertically grown Co_3O_4 NS and their reasonable distribution contribute to the advantageous multiscale pore structure of the C/Cu@Co_3O_4 microspheres. The corresponding electrode still has a reversible charge-specific capacity of ~907 mA h g^{-1} after 200 cycles. Fig. 5e depicts its long-term cycling curve to evaluate the cyclic lifetime of the electrode. The specific capacity of the C/Cu@Co_3O_4 electrode gradually increases and then stabilizes at ~944 mA h g^{-1} after decaying the initial few cycles. Conversely, the reversible capacity of the Co_3O_4 NS electrode decreases significantly during the first 60 cycles owing to the greater volume expansion/contraction of the electrode at a high current density, which leads to a possible rupture, peeling, and reorganization of the external SEI films [61]. However, the reversible capacity of the Co_3O_4 NS electrode gradually increases after about the 60th cycle, which can be attributed to the gradual activation of the active material and the creation of the polymer gel-like film [58,59]. To investigate the capacity contribution of the C/Cu substrate and Co_3O_4 NS during charge/discharge cycling, the cycling performances of C/Cu electrodes were examined at current densities of 100 and 1000 mA g^{-1}, respectively. Fig. S13 shows that the C/Cu electrode shows the specific capacities of only 266 and 173 mA h g^{-1} after 200 cycles at 100 mA g^{-1} and 800 cycles at 1000 mA g^{-1}, respectively, much lower than those of the Co_3O_4 NS electrode. Therefore, Co_3O_4 NS mainly contributes to the specific capacity of the C/Cu@Co_3O_4 electrode. However, the C/Cu electrode presents better cycling stability under low and high current densities. Thus, C/Cu@Co_3O_4 electrodes have both the high specific capacity inherent in Co_3O_4 NS and significantly improved cycling stability compared with Co_3O_4 NS electrodes. The excellent cycling performance of C/Cu@Co_3O_4 can be attributed to the robust and unique structure of C/Cu@Co_3O_4 which is responsible for its exceptional cycling performance, where the vertically grown Co_3O_4 NS is uniformly distributed on the inner and outer carbon walls of the C/Cu microspheres. By the interconnected pore network of C/Cu substrates and the ample space between the vertically grown Co_3O_4 NS, a consistent Li^+ flux can be generated, and uniform electrochemical reactions of Li^+ can occur on the interface of the active material [62]. Fig. S14a, b depict the SEM images of Co_3O_4 NS and C/Cu@Co_3O_4 electrodes in half-cells after cycling. Many irregular and rough island-like lithium aggregates were observed on the surface of the Co_3O_4 NS electrode after 200 cycles at 100 mA g^{-1} (Fig. S14a). The lithium deposition can be attributed to the disordered stacking between the Co_3O_4 NS, leading to uneven plating of lithium on the surface of NSs. Consequently, the gradual deposition of lithium onto the NS results in the formation of lithium aggregates that resemble irregular islands. The C/Cu@Co_3O_4 microspheres possess a multiscale porous structure with a reasonable distribution of vertically grown Co_3O_4 NS anchored on the surface as anode materials for LIBs. These microspheres have good structural stability during cycling and can reduce the local effective current density, thus forming a uniform electric field and achieving uniform lithium plating [61]. Therefore, the C/Cu@Co_3O_4 electrode has uniform lithium deposition and exhibits dendrite-free morphology. As shown in Fig. S14b, after 200 cycles at 100 mA g^{-1}, Li was deposited almost uniformly on the surface of the C/Cu@Co_3O_4 electrode, forming a relatively flat and smooth lithium layer. Consequently, the C/Cu@Co_3O_4 electrode shows an excellent cycling performance.

We investigated the CV curves of the C/Cu@Co_3O_4 electrode at various scan rates (Fig. 6a) to further analyze the lithium storage mechanism in the electrode. These curves retain the same shape as the scan rate increases, but their width widens. Due to the polarization effect, the reduction peak shifts downward, and the oxidation peak moves upward in the CV curves with increasing scan rates. This is caused by the unavoidable resistance between potential and current [63]. After eliminating the effect of polarization effects, the current could be separated to diffusion-controlled contribution and pseudocapacitive contribution, which are calculated through a series of data processing using Equations (5) and (6) [40]:

$$i = av^b, \quad (5)$$

$$\log(i) = b\log(v) + \log(a), \quad (6)$$

where i and v represent the peak current and scan rate, respectively, and a and b represent constants. The b value can be obtained from the slope of the fitted straight line of $\log(i)$ *vs.* $\log(v)$. The surface-controlled pseudocapacitive process dominates the electrochemical reaction if the b value is close to 1.0. If the b value is near 0.5, the diffusion-controlled Li^+ insertion process dominates the electrochemical reaction. The b values calculated for the anodic and cathodic processes are 0.76 and 0.78 (Fig. 6b), respectively, indicating that both the capacitive and diffusive mechanisms contribute to the capacity of the C/Cu@Co_3O_4 electrode. To quantitatively distinguish the proportional contributions of diffusive capacity and capacitive capacity, Equations (7) and (8) were used [40].

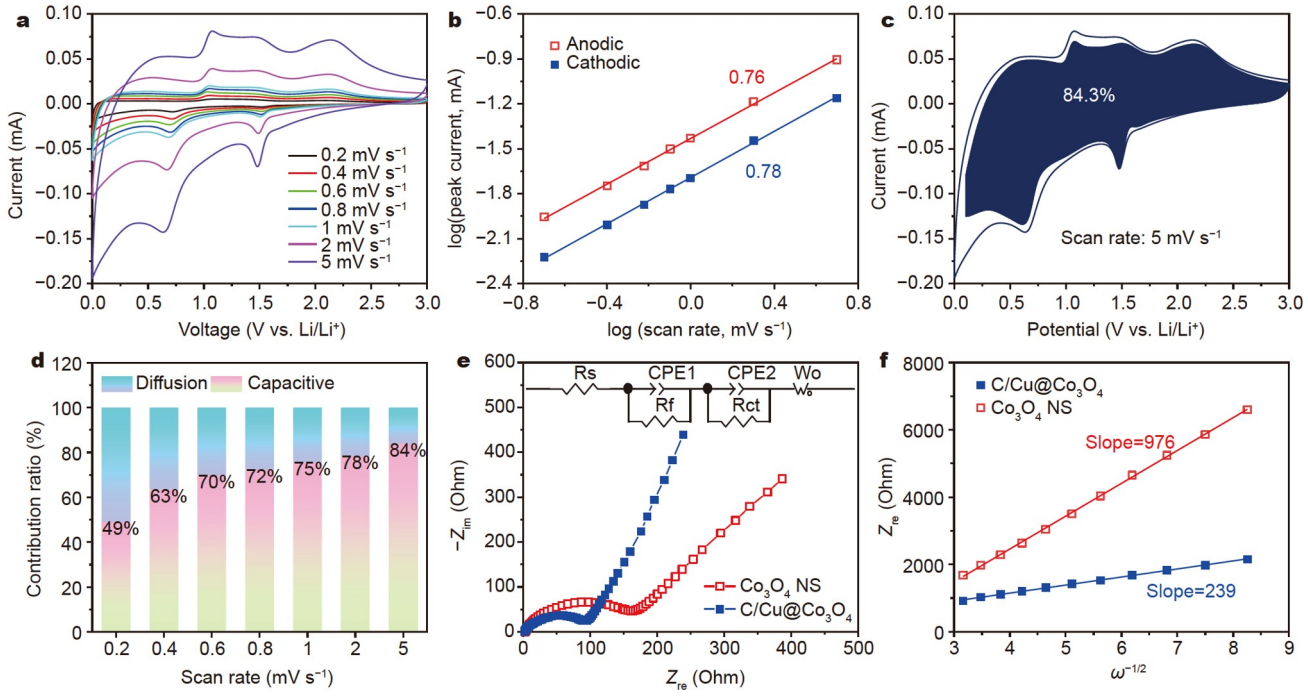

Figure 6 (a) CV curves of the C/Cu@Co_3O_4 electrode at various scan rates. (b) Relationship between the scan rate and the peak current for the C/Cu@Co_3O_4 electrode. (c) Capacitive contribution (navy) to charge storage at a scan rate of 5 mV s^{-1}. (d) Contributions of the capacitive-controlled and diffusion-controlled capacity of the C/Cu@Co_3O_4 electrode at various scan rates. (e) EIS curves of C/Cu@Co_3O_4 and Co_3O_4 NS electrodes after 15 cycles, and (f) the relationship curves between the real parts of the reciprocal square root of angular frequency ($\omega^{-1/2}$) and the impedance (Z_{re}) of the electrodes in the low frequency range. Inset in (e) is the equivalent circuit model.

$$i = k_1 v^{1/2} + k_2 v, \quad (7)$$

$$i/v^{1/2} = k_1 + k_2 v^{1/2}, \quad (8)$$

where k_1 and k_2 represent variable constants, $k_1 v^{1/2}$ is the contribution of diffusivity control, and $k_2 v$ represents the contribution of capacitive control. Furthermore, the darkened area in the voltammogram can be calculated as the specific capacitive contribution using the method introduced by Dunn's group [64]. At a scan rate of 5.0 mV s^{-1}, the capacitive contribution of the C/Cu@Co_3O_4 electrode is 84.3% according to the darkened area in Fig. 6c. The specific capacitive contribution of the C/Cu@Co_3O_4 electrode at various scan rates is shown in Fig. 6d. For scanning rates of 0.2, 0.4, 0.6, 0.8, 1, 2, and 5 mV s^{-1}, the percentage of the capacitive contribution of the C/Cu@Co_3O_4 electrode is obtained to be 49%, 63%, 70%, 72%, 75%, 78%, and 84%, respectively. As the scan rates increase, the capacitive contribution of the C/Cu@Co_3O_4 electrode gradually rises. Thus, diffusive capacity dominates the capacity composition of the C/Cu@Co_3O_4 electrode at a lower scan rate. However, at a higher scan rate, the capacitive contribution of the C/Cu@Co_3O_4 electrode rises, indicating that the distinctive structure of C/Cu@Co_3O_4 facilitates surface-induced lithium storage at high current densities. Specifically, the introduction of the C/Cu carbon substrate, which provides a large specific surface area and enhances the conductivity for the surface-controlled capacitive process, is primarily responsible for the high capacitive contribution [65].

The charge transfer behavior and Li^+ diffusion kinetics in the electrode materials were evaluated using EIS tests. Fig. 6e describes the EIS curves of C/Cu@Co_3O_4 and Co_3O_4 NS cells after 15 cycles. Due to the rebalancing between SEI film resistance and charge transfer, all EIS curves show a semicircle in both the high and mid-frequency ranges and a linear Warburg tail in the low-frequency range, attributed to the solid-state diffusion of Li^+ in the electrode material [66]. The semicircles in the mid- and high-frequency ranges are separated into charge transfer resistance (R_{ct}) and SEI resistance (R_f) *via* the equivalent circuit model in Fig. 6e, and the fitting results are presented in Table S2 [67]. After 15 cycles, the SEI film of the electrode material was fully formed and stabilized, and the R_{ct} value of the C/Cu@Co_3O_4 electrode (67.3 Ω) was substantially lower than that of the Co_3O_4 NS electrode (126.5 Ω), showing that the C/Cu@Co_3O_4 electrode has a higher charge transfer rate.

To further analyze the diffusion behavior of Li^+, the diffusion coefficient of Li^+ (D_{Li}) in the electrode can be investigated as follows [66]:

$$D_{Li} = R^2T^2/2A^2n^4F^4C^2\sigma^2, \quad (9)$$

where A is the surface area of the electrode, C is the concentration of Li^+, F is the Faraday constant, n is the number of electrons involved in the reaction, T is the absolute temperature, and R is the gas constant. Additionally, σ is the Warburg coefficient, which can be calculated from the slope of the straight line fitted between $\omega^{-1/2}$ and Z_{re} in the low-frequency ranges. Specifically, this can be determined by Equations (10) and (11):

$$Z_{re} = R + \sigma\omega^{-1/2}, \quad (10)$$

$$\omega = 2\pi f. \quad (11)$$

Notably, D_{Li} is positively correlated with $1/\sigma^2$. From the fitting results in Fig. 6f, the slope for the C/Cu@Co_3O_4 electrode is 239, which is lower than that of the Co_3O_4 NS electrode (976). Consequently, under the same circumstances, the diffusion coefficient of Li^+ of the C/Cu@Co_3O_4 electrode is 16.7 times higher than that of the Co_3O_4 NS electrode. This enhanced ion diffusion coefficient is attributed to the multiscale pore structure

and uniform distribution of Co_3O_4 NS on the C/Cu microspheres. This unique structure provides numerous diffusion channels, shortens the distance of Li^+ diffusion, and enlarges the contact area between the electrolyte and the electrode. The vertically grown mesoporous Co_3O_4 NS anchored on the porous microspheres provides sufficient pores for Li^+ transport and prevents the aggregation of Co_3O_4 NS during the charging/discharging cycles. Simultaneously, the C/Cu matrix considerably improves the conductivity of the electrode materials and facilitates the diffusion kinetics of Li^+ [68].

As shown in Fig. S15 and Table S3, the electrochemical performance of the C/Cu@Co_3O_4 electrode is superior to those of reported Co_3O_4/carbon materials in various forms. Regarding lithium storage, the C/Cu@Co_3O_4 electrodes developed in our work exhibit outstanding long-cycle stability, high reversible charge-specific capacity, and excellent rate performance, owing to the synergistic influence of the hierarchical structure of the C/Cu microspheres and the reasonably distributed Co_3O_4 NS. First, the multiscale structure of microspheres provides a large specific surface area, which enlarges the contact area between the electrolyte and the electrode and accelerates the diffusion of Li^+, thereby accelerating the redox reaction. Second, the network of the interconnected pores of microspheres and the sufficient space between the interlaced Co_3O_4 NS can buffer the volume expansion/contraction of the electrode during discharge/charge cycles. Finally, due to the strong interaction force between the C/Cu matrix and Co_3O_4 NS, the exfoliation and agglomeration of Co_3O_4 can be effectively impeded during the charging and discharging processes. Therefore, the C/Cu@Co_3O_4 electrode demonstrates enhanced electrochemical performance.

CONCLUSIONS

In this work, composite microspheres firmly coated with vertically aligned and interlaced Co_3O_4 NS were synthesized using C/Cu microspheres with a multiscale structure as the substrates. When used as an anode material for LIBs, the interpenetrating porous structure of C/Cu@Co_3O_4 microspheres facilitates the penetration of electrolyte, accelerates charge transfer, increases the electrolyte/electrode interface, promotes fast reaction, and mitigates the volume expansion/contraction of the electrode during discharge/charge cycles. Moreover, the N- and Cu-doped chitin-derived carbon substrate facilitates the conduction of electrons and enhances the electrical conductivity of the electrode material. Owing to exceptional properties, the C/Cu@Co_3O_4 microspheres exhibit superior long-cycle stability, high reversible charge-specific capacity, and excellent rate performance when applied as anode materials for LIBs, with the specific capacity of ~907 mA h g^{-1} at a current density of 100 mA g^{-1} after 200 cycles and ~944 mA h g^{-1} at a current density of 1000 mA g^{-1} after 800 cycles. Therefore, the present research establishes a promising method for designing carbon/TMO hybrids with a hierarchical structure as high-performance electrode materials.

Received 18 August 2023; accepted 8 October 2023; published online 22 November 2023

1 Chen Z, Danilov DL, Eichel RA, *et al.* Porous electrode modeling and its applications to Li-ion batteries. Adv Energy Mater, 2022, 12: 2201506
2 Jiang L, Sheng L, Fan Z. Biomass-derived carbon materials with structural diversities and their applications in energy storage. Sci China Mater, 2018, 61: 133–158
3 Kang MS, Heo I, Kim S, *et al.* High-areal-capacity of micron-sized silicon anodes in lithium-ion batteries by using wrinkled-multilayered-graphenes. Energy Storage Mater, 2022, 50: 234–242
4 Chen X, Li H, Yan Z, *et al.* Structure design and mechanism analysis of silicon anode for lithium-ion batteries. Sci China Mater, 2019, 62: 1515–1536
5 Zhou J, Xu S, Kang Q, *et al.* Iron oxide encapsulated in nitrogen-rich carbon enabling high-performance lithium-ion capacitor. Sci China Mater, 2020, 63: 2289–2302
6 Ata-ur-Rehman , Iftikhar M, Latif S, *et al.* Current advances and prospects in NiO-based lithium-ion battery anodes. Sustain Energy Technol Assessments, 2022, 53: 102376
7 Xu H, Zhu G, Hao B. Metal-organic frameworks derived flower-like Co_3O_4/nitrogen doped graphite carbon hybrid for high-performance sodium-ion batteries. J Mater Sci Tech, 2019, 35: 100–108
8 Dong Y, Jiang X, Mo J, *et al.* Hollow CuO nanoparticles in carbon microspheres prepared from cellulose-cuprammonium solution as anode materials for Li-ion batteries. Chem Eng J, 2020, 381: 122614
9 Liang F, Dong H, Ji Z, *et al.* Temperature-dependent synthesis of SnO_2 or Sn embedded in hollow porous carbon nanofibers toward customized lithium-ion batteries. Sci China Mater, 2023, 66: 1736–1746
10 Feng Y, Shu N, Xie J, *et al.* Carbon-coated Fe_2O_3 hollow sea urchin nanostructures as high-performance anode materials for lithium-ion battery. Sci China Mater, 2021, 64: 307–317
11 Wang J, Yang N, Tang H, *et al.* Accurate control of multishelled Co_3O_4 hollow microspheres as high-performance anode materials in lithium-ion batteries. Angew Chem Int Ed, 2013, 52: 6417–6420
12 Zhou Y, Wang C, Chen F, *et al.* Synchronous constructing ion channels and confined space of Co_3O_4 anode for high-performance lithium-ion batteries. Nano Res, 2022, 15: 6192–6199
13 Liu H, Liu X, Wang S, *et al.* Transition metal based battery-type electrodes in hybrid supercapacitors: A review. Energy Storage Mater, 2020, 28: 122–145
14 Cong L, Zhang S, Zhu H, *et al.* Structure-design and theoretical-calculation for ultrasmall Co_3O_4 anchored into ionic liquid modified graphene as anode of flexible lithium-ion batteries. Nano Res, 2021, 15: 2104–2111
15 Cheong JY, Chang JH, Cho SH, *et al.* High-rate formation cycle of Co_3O_4 nanoparticle for superior electrochemical performance in lithium-ion batteries. Electrochim Acta, 2019, 295: 7–13
16 Wan P, Si Y, Zhu S, *et al.* Ultrasmall Co_3O_4 nanoparticles as a long-lived high-rate lithium-ion battery anode. Dalton Trans, 2023, 52: 3270–3274
17 Chen M, Xia X, Yin J, *et al.* Construction of Co_3O_4 nanotubes as high-performance anode material for lithium ion batteries. Electrochim Acta, 2015, 160: 15–21
18 Wang J, Wang C, Zhen M. Template-free synthesis of multifunctional Co_3O_4 nanotubes as excellent performance electrode materials for superior energy storage. Chem Eng J, 2019, 356: 1–10
19 Li X, Tian X, Yang T, *et al.* Two-pot synthesis of one-dimensional hierarchically porous Co_3O_4 nanorods as anode for lithium-ion battery. J Alloys Compd, 2018, 735: 2446–2452
20 Shin H, Lee WJ. Ultrathin mesoporous shell Co_3O_4 hollow spheres as high-performance electrode materials for lithium-ion batteries. Mater Chem Phys, 2018, 214: 165–171
21 Han X, Han X, Zhan W, *et al.* Preparation of 3D hierarchical porous Co_3O_4 nanostructures with enhanced performance in lithium-ion batteries. RSC Adv, 2018, 8: 3218–3224
22 Cao W, Wang W, Shi H, *et al.* Hierarchical three-dimensional flower-like Co_3O_4 architectures with a mesocrystal structure as high capacity anode materials for long-lived lithium-ion batteries. Nano Res, 2018, 11: 1437–1446
23 Wang B, Lu XY, Wong KY, *et al.* Facile solvothermal synthesis and superior lithium storage capability of Co_3O_4 nanoflowers with multi-scale dimensions. Mater Chem Front, 2017, 1: 468–476
24 Xie Q, Song R, Zhao P, *et al.* In-plane porous Co_3O_4 nanosheet assembled 3D hierarchical clusters grown on stainless steel mesh as binder-free anodes for high performance lithium ion batteries. J Mater

Chem A, 2018, 6: 8388–8395
25 Li A, Zhong M, Shuang W, *et al.* Facile synthesis of Co_3O_4 nanosheets from MOF nanoplates for high performance anodes of lithium-ion batteries. Inorg Chem Front, 2018, 5: 1602–1608
26 Du H, Yuan C, Huang K, *et al.* A novel gelatin-guided mesoporous bowknot-like Co_3O_4 anode material for high-performance lithium-ion batteries. J Mater Chem A, 2017, 5: 5342–5350
27 Zhao J, Wang J, Bi R, *et al.* General synthesis of multiple-cores@multiple-shells hollow composites and their application to lithium-ion batteries. Angew Chem Int Ed, 2021, 60: 25719–25722
28 Sun Y, Huang F, Li S, *et al.* Novel porous starfish-like Co_3O_4@nitrogen-doped carbon as an advanced anode for lithium-ion batteries. Nano Res, 2017, 10: 3457–3467
29 Etacheri V, Hong CN, Tang J, *et al.* Cobalt nanoparticles chemically bonded to porous carbon nanosheets: A stable high-capacity anode for fast-charging lithium-ion batteries. ACS Appl Mater Interfaces, 2018, 10: 4652–4661
30 Zhu J, Tu W, Pan H, *et al.* Self-templating synthesis of hollow Co_3O_4 nanoparticles embedded in N,S-dual-doped reduced graphene oxide for lithium ion batteries. ACS Nano, 2020, 14: 5780–5787
31 Yao Y, Zhu Y, Zhao S, *et al.* Halide ion intercalated electrodeposition synthesis of Co_3O_4 nanosheets with tunable pores on graphene foams as free-standing and flexible Li-ion battery anodes. ACS Appl Energy Mater, 2018, 1: 1239–1251
32 Chen YM, Yu L, Lou XWD. Hierarchical tubular structures composed of Co_3O_4 hollow nanoparticles and carbon nanotubes for lithium storage. Angew Chem Int Ed, 2016, 55: 5990–5993
33 Zhang K, Xiong F, Zhou J, *et al.* Universal construction of ultrafine metal oxides coupled in N-enriched 3D carbon nanofibers for high-performance lithium/sodium storage. Nano Energy, 2020, 67: 104222
34 Wang X, Tang Y, Shi P, *et al.* Self-evaporating from inside to outside to construct cobalt oxide nanoparticles-embedded nitrogen-doped porous carbon nanofibers for high-performance lithium ion batteries. Chem Eng J, 2018, 334: 1642–1649
35 Zhang CL, Lu BR, Cao FH, *et al.* Hierarchically structured Co_3O_4@carbon porous fibers derived from electrospun ZIF-67/PAN nanofibers as anodes for lithium ion batteries. J Mater Chem A, 2018, 6: 12962–12968
36 Wang B, Ryu J, Choi S, *et al.* Folding graphene film yields high areal energy storage in lithium-ion batteries. ACS Nano, 2018, 12: 1739–1746
37 Zhang X, Liu C, Wang R. Self-assembly of corn-like Co_3O_4 from nanoparticles induced by graphene wrinkles and its application in lithium ion batteries. Sustain Energy Fuels, 2021, 5: 2469–2476
38 Chen Y, Wang Y, Wang Z, *et al.* Densification by compaction as an effective low-cost method to attain a high areal lithium storage capacity in a CNT@Co_3O_4 sponge. Adv Energy Mater, 2018, 8: 1702981
39 Gao L, Ma J, Li S, *et al.* 2D ultrathin carbon nanosheets with rich N/O content constructed by stripping bulk chitin for high-performance sodium ion batteries. Nanoscale, 2019, 11: 12626–12636
40 Zhang K, He Q, Xiong F, *et al.* Active sites enriched hard carbon porous nanobelts for stable and high-capacity potassium-ion storage. Nano Energy, 2020, 77: 105018
41 Sun X, Wang Z, Ai X, *et al.* CuO nanosheets embedded on carbon microspheres as high-performance anode material in lithium-ion batteries. Sci China Mater, 2023, 66: 3026–3038
42 Duan B, Zheng X, Xia Z, *et al.* Highly biocompatible nanofibrous microspheres self-assembled from chitin in NaOH/urea aqueous solution as cell carriers. Angew Chem Int Ed, 2015, 54: 5152–5156
43 Ren H, Yu R, Qi J, *et al.* Hollow multishelled heterostructured anatase/TiO_2(B) with superior rate capability and cycling performance. Adv Mater, 2019, 31: 1805754
44 Wang J, Gao B, Zhang L, *et al.* Controlled synthesis of porous Co_3O_4–C hybrid nanosheet arrays and their application in lithium ion batteries. RSC Adv, 2014, 4: 30573–30578
45 Wang X, Guan H, Chen S, *et al.* Self-stacked Co_3O_4 nanosheets for high-performance lithium ion batteries. Chem Commun, 2011, 47: 12280–12282
46 Cheng Q, Huang M, Xiao A, *et al.* Recyclable nitrogen-containing chitin-derived carbon microsphere as sorbent for neonicotinoid residues adsorption and analysis. Carbohydrate Polyms, 2021, 260: 117770
47 Zou G, Hou H, Foster CW, *et al.* Advanced hierarchical vesicular carbon co-doped with S, P, N for high-rate sodium storage. Adv Sci, 2018, 5: 1800241
48 Yang J, Ju Z, Jiang Y, *et al.* Enhanced capacity and rate capability of nitrogen/oxygen dual-doped hard carbon in capacitive potassium-ion storage. Adv Mater, 2018, 30: 1700104
49 Chen Z, Hou Z, Xu W, *et al.* Ultrafine CuO nanoparticles decorated activated tube-like carbon as advanced anode for lithium-ion batteries. Electrochim Acta, 2019, 296: 206–213
50 Li HH, Zhou L, Zhang LL, *et al.* Co_3O_4 nanospheres embedded in a nitrogen-doped carbon framework: An electrode with fast surface-controlled redox kinetics for lithium storage. ACS Energy Lett, 2017, 2: 52–59
51 Liu T, Zhang L, You W, *et al.* Core-shell nitrogen-doped carbon hollow spheres/Co_3O_4 nanosheets as advanced electrode for high-performance supercapacitor. Small, 2018, 14: 1702407
52 Xiang X, Pan P, Li P, *et al.* Preparation of a N-doped Si/Cu/C anode for high-performance lithium-ion batteries. Sustain Energy Fuels, 2023, 7: 1041–1050
53 Xu C, Xia T, Wang C, *et al.* Stable and fast Si-M-C ternary anodes enabled by interfacial engineering. J Power Sources, 2022, 530: 231290
54 Wu S, Zhang Z, Lan M, *et al.* Lithiophilic Cu-CuO-Ni hybrid structure: Advanced current collectors toward stable lithium metal anodes. Adv Mater, 2018, 30: 1705830
55 Dwivedi PK, Nair A, Mehare RS, *et al.* Experimental and theoretical investigations of the effect of heteroatom-doped carbon microsphere supports on the stability and storage capacity of nano-Co_3O_4 conversion anodes for application in lithium-ion batteries. Nanoscale Adv, 2020, 2: 2914–2924
56 Pu F, Bai Y, Lv J, *et al.* Yolk-shell Cu_2O@CuO-decorated RGO for high-performance lithium-ion battery anode. Energy & Environ Mater, 2022, 5: 253–260
57 Yu M, Sun Y, Du H, *et al.* Hollow porous carbon spheres doped with a low content of Co_3O_4 as anode materials for high performance lithium-ion batteries. Electrochim Acta, 2019, 317: 562–569
58 Zou F, Hu X, Li Z, *et al.* MOF-derived porous ZnO/$ZnFe_2O_4$/C octahedra with hollow interiors for high-rate lithium-ion batteries. Adv Mater, 2014, 26: 6622–6628
59 Meng J, Liu Z, Niu C, *et al.* General oriented assembly of uniform carbon-confined metal oxide nanodots on graphene for stable and ultrafast lithium storage. Mater Horiz, 2018, 5: 78–85
60 Zhang J, Yu A. Nanostructured transition metal oxides as advanced anodes for lithium-ion batteries. Sci Bull, 2015, 60: 823–838
61 Li L, Dong G, Xu Y, *et al.* H_3IDC-assisted synthesis of mesoporous ultrafine Co_3O_4/N-doped carbon nanowires as a high rate and long-life anode for lithium-ion batteries. J Alloys Compd, 2020, 818: 152826
62 Huang G, Lou P, Xu GH, *et al.* Co_3O_4 nanosheet decorated nickel foams as advanced lithium host skeletons for dendrite-free lithium metal anode. J Alloys Compd, 2020, 817: 152753
63 Pu X, Zhao D, Fu C, *et al.* Understanding and calibration of charge storage mechanism in cyclic voltammetry curves. Angew Chem Int Ed, 2021, 60: 21310–21318
64 Brezesinski T, Wang J, Polleux J, *et al.* Templated nanocrystal-based porous TiO_2 films for next-generation electrochemical capacitors. J Am Chem Soc, 2009, 131: 1802–1809
65 Zhang S, Wang G, Zhang Z, *et al.* 3D graphene networks encapsulated with ultrathin SnS nanosheets@hollow mesoporous carbon spheres nanocomposite with pseudocapacitance-enhanced lithium and sodium storage kinetics. Small, 2019, 15: 1900565
66 Ni D, Sun W, Wang Z, *et al.* Heteroatom-doped mesoporous hollow carbon spheres for fast sodium storage with an ultralong cycle life. Adv Energy Mater, 2019, 9: 1900036
67 Deng X, Xie K, Li L, *et al.* Scalable synthesis of self-standing sulfur-doped flexible graphene films as recyclable anode materials for low-cost sodium-ion batteries. Carbon, 2016, 107: 67–73
68 Yu WJ, Zhang L, Hou PX, *et al.* High reversible lithium storage capacity and structural changes of Fe_2O_3 nanoparticles confined inside carbon

nanotubes. Adv Energy Mater, 2016, 6: 1501755

Acknowledgements This work was financially supported by the Key Research and Development Program of Hubei Province (2020BCA079) and the National Natural Science Foundation of China (52173106). The authors thank the Core Facility of Wuhan University for characterizations.

Author contributions Sun X conceived and designed the experiments, prepared and characterized the samples, analyzed the experimental data, and wrote the original manuscript. Zhang J assembled batteries. Zhang H helped analyze the data. Cao Y and Zhou J reviewed and edited the manuscript. Zhou J supervised the project.

Conflict of interest The authors declare that they have no conflict of interest.

Supplementary information Supporting data are available in the online version of the paper.

Xun Sun received his MS degree in polymer chemistry and physics from Fujian Normal University in 2018. He is currently pursuing his PhD degree at Wuhan University, where his current research focuses on natural polymeric materials for energy storage and conversion.

Jun Zhang received her BS degree (2022) in applied chemistry from China University of Petroleum. She is pursuing a Master's degree at the College of Chemistry and Molecular Sciences, Wuhan University. Her research interests mainly focus on hard carbon anodes for sodium-ion batteries.

Huaran Zhang received his BS degree in chemical engineering and technology from Hefei University of Technology. Now he is pursuing his PhD degree at Wuhan University, and his research focuses on natural polymers-derived carbon materials for energy storage.

Yuliang Cao received his PhD degree (2003) from Wuhan University, and then he worked as a visiting scholar at Pacific Northwest National Laboratory from 2009 to 2011. He is now a professor at the College of Chemistry and Molecular Sciences, Wuhan University. His research interests focus on developing advanced materials (e.g., alloys, transition metal oxides, phosphates, and novel electrolytes) for sodium-ion batteries and LIBs.

Jinping Zhou is a professor at the College of Chemistry and Molecular Sciences, Wuhan University. He received his PhD degree in 2001 from the Department of Chemistry, Wuhan University. His research interests mainly focus on green methods for the modification and fiber spinning of cellulose, and functional materials based on natural polymers.

C/Cu多孔微球固载Co_3O_4纳米片作为锂离子电池的高性能负极材料

孙逊[1,2†], 张珺[1†], 张华然[1], 曹余良[1*], 周金平[1*]

摘要 过渡金属氧化物(TMOs)用作电极材料时, 会在循环过程中产生严重的体积变化, 并且其自身的导电率也较低, 因此它的电化学性能较差. 设计和开发独特的TMOs纳米结构并将其与导电碳基底相结合是改善其电化学性能的有效策略. 本工作中, 我们设计了一种C/Cu多孔微球, 并通过原位合成在碳壁上垂直生长Co_3O_4纳米片. 作为导电基底, C/Cu多孔微球提供了多尺度孔隙网络和大的电极/电解质接触界面, 显著改善了电子和离子扩散动力学. 原位合成的Co_3O_4纳米片牢牢地固定在碳壁上, 从而提高了复合微球在长期循环中的结构稳定性. 得益于独特的结构特征, 用作锂离子电池负极材料的C/Cu@Co_3O_4复合多孔微球表现出优异的倍率性能、高充电比容量和出色的循环稳定性.

